PHOTONICS Research

High-performance, low-power, and flexible ultraviolet photodetector based on crossed ZnO microwires p-n homojunction

Shulin Sha,[1] Kai Tang,[1] Maosheng Liu,[1] Peng Wan,[1] Chenyang Zhu,[1] Daning Shi,[1] Caixia Kan,[1,2] and Mingming Jiang[1,*]

[1]College of Physics, MIIT Key Laboratory of Aerospace Information Materials and Physics, Key Laboratory for Intelligent Nano Materials and Devices, Nanjing University of Aeronautics and Astronautics, Nanjing 211106, China
[2]e-mail: cxkan@nuaa.edu.cn
*Corresponding author: mmjiang@nuaa.edu.cn

Received 13 September 2023; revised 20 December 2023; accepted 9 January 2024; posted 9 January 2024 (Doc. ID 505839); published 18 March 2024

Low-power, flexible, and integrated photodetectors have attracted increasing attention due to their potential applications of photosensing, astronomy, communications, wearable electronics, etc. Herein, the samples of ZnO microwires having p-type (Sb-doped ZnO, ZnO:Sb) and n-type (Ga-doped ZnO, ZnO:Ga) conduction properties were synthesized individually. Sequentially, a p-n homojunction vertical structure photodiode involving a single ZnO:Sb microwire crossed with a ZnO:Ga microwire, which can detect ultraviolet light signals, was constructed. When exposed under 360 nm light illumination at −0.1 V, the proposed photodiode reveals pronounced photodetection features, including a largest on/off ratio of 10^5, responsivity of 2.3 A/W, specific detectivity of ∼6.5×10^{13} Jones, noise equivalent power of 4.8×10^{-15} W $Hz^{-1/2}$, and superior photoelectron conversion efficiency of ∼7.8%. The photodiode also exhibits a fast response/recovery time of 0.48 ms/9.41 ms. Further, we propose a facile and scalable construction scheme to integrate a p-ZnO:Sb ⊗ n-ZnO:Ga microwires homojunction component into a flexible, array-type detector, which manifests significant flexibility and electrical stability with insignificant degradation. Moreover, the as-constructed array unit can be integrated into a practical photoimaging system, which demonstrates remarkable high-resolution single-pixel imaging capability. The results represented in this work may supply a workable approach for developing low-dimensional ZnO-based homojunction optoelectronic devices with low-consumption, flexible, and integrated characteristics.

https://doi.org/10.1364/PRJ.505839

1. INTRODUCTION

In recent years, the flexible and integrated ultraviolet photodetector (UV PD) has become a crucial active component for photosensing, optical communications, wearable devices, foldable displays, etc. [1–5]. To satisfy the ever-increasing demands of realistic applications, the construction of flexible and integrated photodiodes should necessarily mandate advantages such as low energy consumption, low dark current, fast response time, high mechanical stability, etc. [6–8]. In previous studies, low-dimensional organic and inorganic materials, such 0D quantum dots, 1D micro-/nanostructures, and 2D layered materials have been extensively used to fabricate flexible and integrated devices [9–15]. However, the PDs based on 0D and 2D materials have several drawbacks owing to material intrinsic problems and complex fabrication techniques [16,17]. For example, the solution-synthesized 0D materials are prone to problems such as instability, low photogenerated charge carrier density, poor charge transport, and so on, which seriously hinder further applications of quantum dot-based flexible photovoltaic devices [18–21]. Additionally, although significant progress has been achieved in developing flexible optoelectronic devices based on the 2D layered materials. The presence of poorer light absorption, large-scale, complex preparation process, difficult transfer, poor ductility, etc., also makes them unable to carry out large-area practical applications [22–24]. In contrast, 1D micro-/nanostructure materials have been widely applied in flexible detectors because of their superior mechanical stability, high carrier mobility, high surface-to-volume ratio, and simple synthesis [17,25]. In particular, assembling these 1D micro-/nanostructures into highly ordered arrays as ideal building blocks can realize the low-power, flexibility, and integration practical applications for novel optoelectronic devices [26–28].

ZnO, an important third-generation semiconductor, has been widely considered as potential material for the construction of UV PDs owing to the low cost, abundance of raw

materials, nontoxicity, large bandgap of 3.37 eV, and high exciton binding energy of 60 meV [29–31]. Low-dimensional ZnO, including nanofibers, microwires (MWs), nanowires, and so on, has attracted extensive scientific interest in flexible detectors owing to their large length/diameter ratio, miniaturization, and flexibility. Generally, there are three types of detectors: metal-semiconductor-metal (MSM); Schottky; and p-n junction [1,32–35]. The limitations of a typical MSM structure detector such as complex metal electrode contacts, large operating voltage, and low photoresponse would inevitably restrict the development toward low-power consumption, flexibility, and integration [1,32,36,37]. Compared with photovoltaic p–n junction detectors, the traditional Schottky devices usually suffer from numerous bottlenecks, such as serious absorption of metal electrodes, relatively thinner depletion layer, and photocarriers transporting barriers. These shortcomings severely hinder the further application of Schottky-based PDs [38–40]. The realization of p–n junction photodiodes has received widespread attention owing to its excellent photodetection properties. Because of the lattice mismatch, heterojunction interface discontinuity of energy levels, etc., p–n heterojunctions usually have numerous defects, such as trapping states, large leakage current, surface defects, and high strains, thus bringing about economic difficulties in constructing high-performance heterojunction photodiodes [41–44]. Currently, the achievement of ZnO-based homojunction photodiodes has been blocked by the presence of high-quality p-type ZnO. Developing ZnO homojunction UV detectors that meet the requirements of low power consumption, high-performance, flexibility, integrability, and practical applicability remains a long-term and arduous task [4,45,46].

In this work, the sample of Ga-doped ZnO (ZnO:Ga) MWs showing n-type conductivity was synthesized individually, while the product of p-type conductivity ZnO MWs, which were doped with Sb-dopant (ZnO:Sb), was also obtained. The conducting properties were subsequently further verified using single MW-based field-effect transistors (FETs). A vertically structured p-n homojunction containing ZnO:Sb MW crossed with ZnO:Ga MW was constructed, showing excellent UV photodetection capability. When operated under 360 nm light irradiation at −0.1 V, the largest responsivity, detectivity, on/off ratio, noise equivalent power, and photoelectron conversion efficiency can reach ∼2.3 A/W, $\sim 6.5 \times 10^{13}$ Jones, 10^5, 4.8×10^{-15} W $Hz^{-1/2}$, and 7.8%, respectively. The device also exhibited a fast rise/decay speed ($\tau_r/\tau_d \sim 0.48/79.41$ ms). Further, the PD could be integrated into large-scale flexible optoelectronic arrays, which shows small degradation in the photocurrent after 400 bending cycles. Interestingly, the array unit as a pixel sensor exhibits its huge potential for UV imaging. This work offers a novel approach to design and fabricate high-performance, low-power, flexible, and integrable optoelectronic devices.

2. EXPERIMENTAL SECTION

A. Preparation of ZnO:Ga MW and ZnO:Sb MW

In the present study, the sample of MWs was synthesized using a chemical vapor deposition (CVD) method [47,48]. The rational preparation of samples with tunable n-type conductivity is available using Ga_2O_3 as the doping source. In the synthesis process of individual ZnO:Ga MWs, the precursor mixture containing ZnO, Ga_2O_3, and graphite (C) powder with a weight ratio of 9:1:10 served as source materials. Using the CVD method, individual ZnO:Ga MWs were successfully obtained. Compared with the preparation of n-type ZnO:Ga MW, the Sb element is commonly used to substitute Zn to induce p-type conductivity. The experimental scheme has been illustrated in our previous literature [29,49]. In the synthesis process of individual ZnO:Sb MW, a powder mixture of ZnO, Sb_2O_3, and C high purity powder (99.99%) in a weight ratio of approximately 9:1:10 was used as the source.

B. Fabrication of MW-Based FET and Homojunction Device

To investigate the electronic transport properties of CVD-prepared samples, an MW-based FET was fabricated by combining SiO_2/Si substrate [50]. First, a single MW was mechanically transferred to the cleaned SiO_2/Si wafer. Second, the Ti/Au serving as source and drain electrodes were welded at both the ends of the wire, while the Si substrate was used as the global back gate electrode for the FETs. The corresponding schematic illustration of the single MW-based FET is shown in Fig. 7 in Appendix A.

A representative cross-stacked homojunction device is constructed, which consists of a single p-type ZnO:Sb MW crossed with another n-type ZnO:Ga MW in a cross-shape layout, with each MW having a matching electrode forming an ohmic contact with it, respectively. The detailed fabrication process is summarized as follows: (i) deposition of ∼70 nm thick and ∼30 μm wide Au channel electrode on sapphire using an electron-beam evaporation method (∼0.07 Å/s); (ii) 5 μm thick MgO blocking layers were deposited on both sides of the Au channel electrode (∼0.5 Å/s); (iii) a ZnO:Sb MW was placed on the Au channel electrode; (iv) the other ZnO:Ga MW was then transferred to cross over the ZnO:Sb MW; (v) deposition of ∼5 μm blocking layer on the indium tin oxide (ITO), leaving ∼30 μm of the ITO channel was utilized as the top electrode; and (vi) using ITO to apply pressure to the crossed areas of the MW, which in turn makes good physical contact between the crossed samples. The corresponding schematic diagram of the detailed construction process of the device is shown in Fig. 8 in Appendix B.

C. Characterization

The morphology and structure of CVD-synthesized ZnO:Ga and ZnO:Sb MWs were characterized using a scanning electron microscope (SEM) (TESCAN LAYRA3 GM). The chemical compositions of samples were detected using an energy-dispersive spectrometer (EDS), which was attached to the SEM. The crystal structure of the samples was characterized using X-ray diffraction (XRD) (Malvern Panalytical, Empyrean). The optical photograph of samples was obtained by the microscope (Olympus, BX53M). Photoelectrical properties of the constructed devices were conducted using a semiconductor analyzer (Keysight, B1500A), a light source (EQ99X), and a monochromator (Zolix, Omni-λ200i). The temperature of the device was tested using a handheld thermal imaging camera (FOTRIC 321Q). The response speed of PD devices was

evaluated by connecting the detector with a 10 GΩ resistor. A 365 nm Nd:YAG pulsed laser (Ekspla, NT342) and a digital oscilloscope (Tektronix, DPO 2012B) were used as the light source and data collection, respectively.

3. RESULTS AND DISCUSSION

Figure 1(a) presents the optical photograph of the CVD-prepared ZnO:Sb MW, and a single ZnO:Sb MW sample was successfully picked out by using a facile mechanical transfer method. The corresponding surface morphology of a single ZnO:Sb MW in Fig. 1(b) was obtained by the SEM, where the image displays that the sample exhibits a regular hexagonal prismatic structure, smooth and straight sidewall facets, and sharp edges. The chemical composition of the ZnO:Sb wire was characterized via EDS mapping. As shown in Fig. 1(c), the homogeneous distribution of the Sb element was witnessed, indicating that a high degree of homogeneity of Sb doping was successfully achieved in the synthesis of ZnO:Sb MWs. The phases and crystal structure of CVD-synthesized ZnO:Sb wires were further tested via XRD scanning at a two-diffraction angle ranging from 26° to 40°. The XRD result in Fig. 1(d) shows diffraction peaks positioning at 32.65°, 34.32°, and 36.15°, which are assigned to the (100), (002), and (101) planes, respectively. Thus, the CVD-grown ZnO:Sb MWs are belonging to crystalline hexagonal phase of ZnO (JCPDS No. 36–1451). Further, the diffraction peaks of the samples are relatively sharp without any additional phases, indicating that the synthesized samples have excellent crystalline quality. Further, the microscopic image of the sample [Figs. 9(a) and 9(b) in Appendix C] shows that a high aspect ratio ZnO:Sb MW has uniform morphology and good mechanical flexibility, which benefits its applications in flexible optoelectronic devices.

The electrical transport properties of individual Sb-doped MW were researched using FETs [36]. Figure 1(e) shows a set of typical current and source-drain voltage (I_{ds}–V_{ds}) data under different gate voltage (V_g ranges from −4 V to 4 V). The linear feature of the plotted I_{ds}–V_{ds} curves confirms that the metal electrodes make good ohmic contacts with the single wire. This is further confirmed by the local magnification curve of the I_{ds}–V_{ds} [Fig. 1(f)]. The I_{ds} versus V_g curve for the FET recorded at V_{ds} = 1.2 V is shown in Fig. 1(g). Electrical analysis shows that the conductance of the FET increases (decreases) with increasingly negative (positive) V_g. In consequence, a significant modulation of the typical p-type electrical transport properties of single MW was successfully realized via a simple Sb-doping.

Figure 2(a) shows a representative photograph of CVD-prepared ZnO:Ga MWs, which exhibits outwardly dispersing needle-like growth, indicating an excellent aspect ratio of the synthesized samples. According to the SEM result of a single ZnO:Ga MW in Fig. 2(b), the morphology of wire is a hexagonal prism with a diameter of ∼10 μm. Moreover, the ZnO:Ga MW possesses a uniform morphology throughout its entire length with smooth and flat surfaces. The Ga element distribution is measured in Fig. 2(c) via EDS mapping analysis. It is apparent that the Ga component is uniformly distributed in the ZnO:Ga MWs, indicating that Ga elements can be well incorporated into the ZnO lattice. Figure 2(d) shows the XRD pattern of the samples, in which all the diffraction peaks can be well indexed to the hexagonal wurtzite phase of ZnO. Further, the value of full-width at half-maximum for the (002) plane is 0.071°, manifesting excellent crystal quality of CVD-synthesized samples.

Similarly, the electrical properties of a ZnO:Ga MW can be clarified on the basis of single-wire backgated FETs. Typical I_{ds}

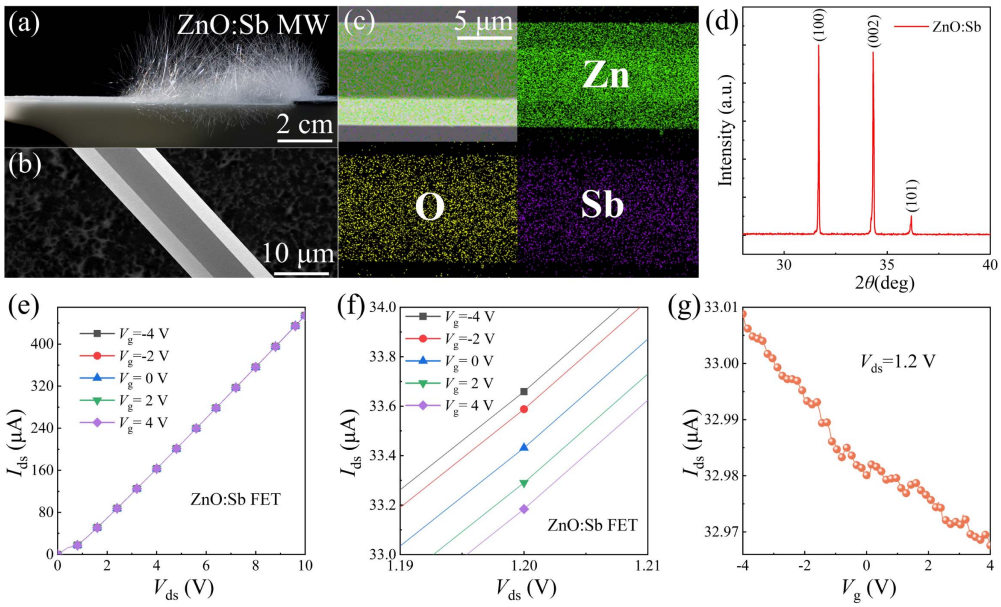

Fig. 1. Characterization of CVD-synthesized ZnO:Sb MWs. (a) Macroscopical photograph of ZnO:Sb MWs. (b) SEM picture of a single ZnO:Sb MW. (c) Elemental mapping images of Zn, O, and Sb species. (d) XRD patterns of ZnO:Sb samples. (e) I_{ds}–V_{ds} curves of the ZnO:Sb MW-based FET at different V_g. (f) Large view of I_{ds}–V_{ds} curves of the ZnO:Sb MW-based FET around V_{ds} = 1.2 V. (g) Transfer characteristic curve I_{ds}–V_g of the ZnO:Sb MW-based FET at V_{ds} = 1.2 V.

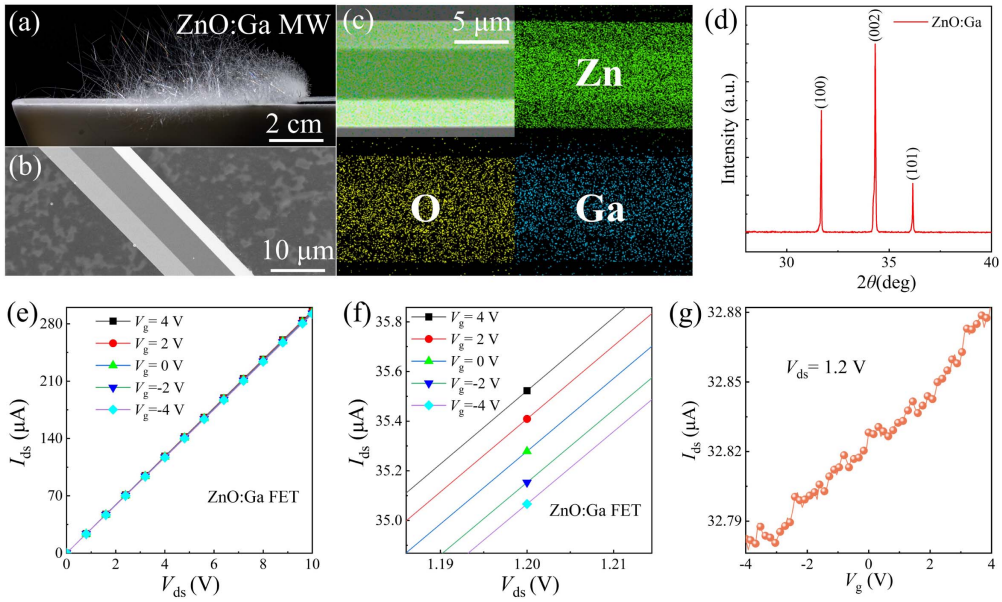

Fig. 2. Characterization of ZnO:Ga MWs. (a) Macroscopical photograph of CVD-synthesized ZnO:Ga MWs. (b) SEM image of a ZnO:Ga MW. (c) Elemental mapping images of Zn, O, and Ga species obtained from a ZnO:Ga MW. (d) XRD patterns of as-synthesized ZnO:Ga MWs. (e) I_{ds}–V_{ds} curves of the ZnO:Ga MW-based FET at different V_g. (f) Large view of I_{ds}–V_{ds} curves of the ZnO:Ga MW-based FET around $V_{ds} = 1.2$ V. (g) I_{ds}–V_g curve of the ZnO:Ga MW FET at $V_{ds} = 1.2$ V.

versus V_{ds} curves under varied V_g are shown in Fig. 2(e). The enlarged result of the output characteristic curve clearly exhibits a typical linear feature of the device [see Fig. 2(f)]. The transport characteristic curve I_{ds}–V_g for the device recorded at $V_{ds} = 1.2$ V is shown in Fig. 2(g). The result shows that the device exhibits a noticeable gating effect, and I_{ds} increases with increasing V_g, which is a typical behavior of the n-type electronic transport properties of our synthesized ZnO:Ga wires [51].

Further, the carrier mobility (μ), conductivity (σ), and carrier density (n_c) in CVD-synthesized ZnO:Sb and ZnO:Ga MWs were estimated by fitting the I_{ds}–V_g curve, respectively. The carrier mobility can be calculated due to $dI_{ds}/dV_g = \mu(C/L^2)V_{ds}$, where C and L are the capacitance and the channel length of single wire, respectively [37]. The capacitance is given by $C \cong 2\pi\varepsilon_0\varepsilon_{SiO_2}L/\ln(2h/d)$, in which ε_0, ε_{SiO_2}, h, and d are the vacuum dielectric constant, relative dielectric constant of SiO_2, thickness of the SiO_2, and diameter of the wire, respectively [36]. The conductivity can be calculated according to $R = \rho L/LS_{cs} = L/L\sigma S_{cs}$, where R, ρ, σ, and S_{cs} are the resistance, resistivity, conductivity, and cross-sectional area of the MW, respectively. The carrier density can be determined by $n_c = \sigma/e\mu$, where e is the elementary charge [30]. Therefore, the carrier mobility, conductivity, and carrier density of ZnO:Sb MWs and ZnO:Ga MWs are as shown in Table 1. The result shows that the corresponding electrical parameters of the ZnO:Ga MW are evidently better than those of ZnO:Sb MW, suggesting that Sb doping can achieve the change of conduction behavior from n- to p-type [47].

Figure 3(a) shows that a representative cross-shape device was constructed by using a vertical structure, which consists of two MWs in a cross-shape layout, with the ITO and Au films

Table 1. Electrical Transport Properties of As-Synthesized Individual ZnO:Sb and ZnO:Ga MWs

Parameters	ZnO:Sb MW	ZnO:Ga MW
Diameter (μm)	10	10
Channel length (μm)	150	150
Carrier mobility ($cm^2\ V^{-1}\ s^{-1}$)	1.13	7.09
Conductivity (S/cm)	0.13	2.80
Carrier density (cm^{-3})	5.65×10^{17}	2.47×10^{18}

acting as contact electrodes for the ZnO:Ga and ZnO:Sb MWs, respectively. An I–V curve in the dark of the constructed device is displayed in Fig. 10(a) in Appendix D. The curve shows that a p-type ZnO:Sb MW crossed with n-type ZnO:Ga MW (p-ZnO:Sb ⊗ n-ZnO:Ga) exhibits clear current rectification characteristic with a turn-on voltage of ~2.0 V, after which the forward current increases rapidly. The inset in Fig. 10(a) in Appendix D shows an optical photograph of the constructed p-ZnO:Sb ⊗ n-ZnO:Ga device. Figure 10(b) (in Appendix D) exhibits that the I–V measurements made on the individual ZnO:Sb and ZnO:Ga MWs show a linear response characteristic of ohmic contacting features. It suggests that the rectification characteristic is mainly attributed to the fabricated crossed-shape MWs device, illustrating that a high-quality homojunction is formed in the physical contact region toward the p-ZnO:Sb ⊗ n-ZnO:Ga interface. To obtain clearer insight into the temperature dependence of the dark current behavior [dark current versus voltage measured at different temperatures as shown in Figs. 11(a)–11(c) in Appendix E], we represent the dark current and the resistance-area product (R_0A) using an Arrhenius plot, as shown in Fig. 3(b). It is found that varying the temperature

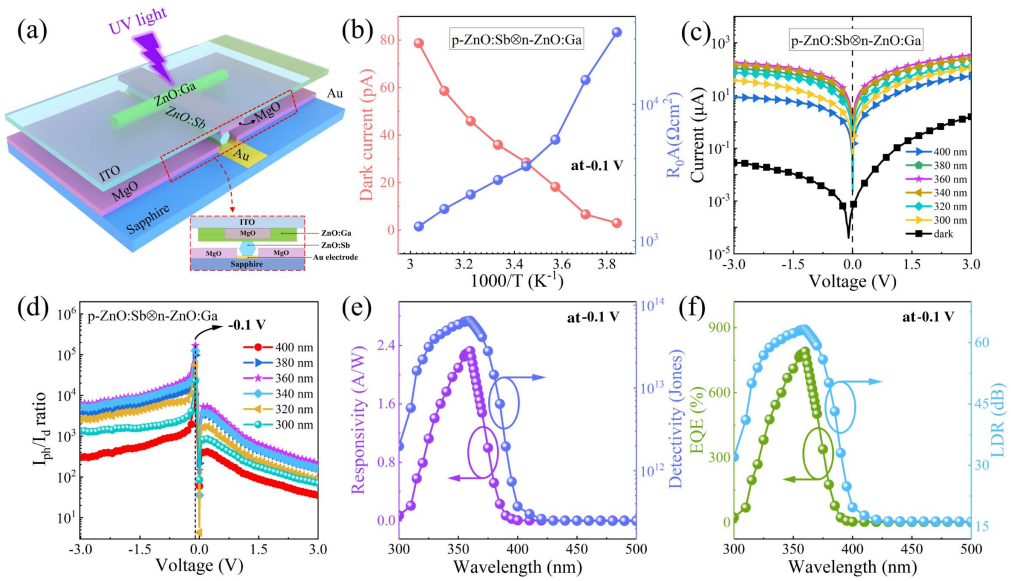

Fig. 3. Characterization of as-constructed p-ZnO:Sb ⊗ n-ZnO:Ga MWs homojunction PD. (a) Schematic observation of the p-ZnO:Sb ⊗ n-ZnO:Ga MWs homostructure device. (b) Arrhenius dark current graph and R_0A plot of the device at different temperature conditions. (c) Logarithmic I–V characteristic curves of the p-ZnO:Sb ⊗ n-ZnO:Ga MWs homostructure device in dark, and upon light illumination with the wavelengths ranging from 300 to 400 nm. (d) Variation of photo-to-dark current ratio $I_{ph} - I_d$ at different wavelengths. (e) Wavelength-dependent R and D^* when evaluated at −0.1 V bias. (f) Wavelength-dependent EQE and LDR when evaluated at −0.1 V bias.

from 260 to 330 K, the dark current exhibits a considerably linear increase. This phenomenon may be derived from the fact that the low temperature would lead to a slower transport efficiency of the interfacial diffusion current, which in turn weakens the dark current. Also, the R_0A product at 330 K is evaluated to about 1269 Ω cm^2. It also increases to 33,670 Ω cm^2 as the temperature reduces to 260 K. The higher value of R_0A results from the tiny junction region interface. In this case, the change through diminishing the surface leakage current would lead to the reduced dark current of as-constructed devices [52].

The photoelectrical properties of the p-ZnO:Sb ⊗ n-ZnO:Ga MW homojunction device were systematically tested under light illumination with different wavelengths. As depicted in Fig. 3(c), the logarithmic I–V characteristic curves under several selected wavelengths (300, 320, 340, 360, 380, and 400 nm) were measured. It can be found that the device has a pronounced photoresponse behavior and shows the largest photocurrent at the wavelength of 360 nm. Figure 3(d) shows that the photo–dark current ratio of the homojunction device can reach as high as ∼1.68 × 10^5 at −0.1 V bias. Additionally, room temperature absorption versus wavelength (λ) plots of ZnO:Ga and ZnO:Sb MWs and the logarithmic I–V characteristic curves of the device in the range of 200–600 nm are shown in Figs. 12(a) and (b) in Appendix F. The absorption edges of the samples appear at 380 nm without any shift for ZnO:Ga and ZnO:Sb samples, indicating that the modulation effect of doping via introducing electron donor (Ga) or acceptor (Sb) elements into the ZnO host crystal on absorption characteristics could be negligible. The optical bandgaps of CVD-grown ZnO:Ga MW and ZnO:Sb MW were calculated to be 3.19 and 3.21 eV, respectively. Compared with bulk ZnO, the deviations could be derived from the self-absorption of CVD-synthesized monocrystalline wirelike structures. Figure 12(c) in Appendix F shows a wavelength-dependent photoresponse at the ultraviolet wavelengths. Owing to the excellent light absorption properties of the samples, the constructed devices exhibit a pronounced photoresponse at the UV wavelengths, with the strongest response occurring at 360 nm.

To quantitatively evaluate the photodetection properties of p-ZnO:Sb ⊗ n-ZnO:Ga homojunction PD, several critical performance parameters, including photocurrent responsivity (R), specific detectivity (D^*), external quantum efficiency (EQE), and linear dynamic range (LDR), were considered. These parameters are described below [40,53,54]:

$$R_{(\lambda)} = \frac{I_{ph} - I_d}{PS}, \tag{1}$$

$$D^* = \frac{R}{\sqrt{2eI_d/S}}, \tag{2}$$

$$\mathrm{EQE} = \frac{hcR_{(\lambda)}}{e\lambda}, \tag{3}$$

$$\mathrm{LDR} = 20\log\left(\frac{I_{ph}}{I_d}\right), \tag{4}$$

where S is the effective irradiated area (1 × 10^{-6} cm^2) of device; P is the incident power intensity (∼0.1 mW/cm^2); I_{ph} and I_d are the photocurrent and dark current of the p-ZnO:Sb ⊗ n-ZnO:Ga homojunction PD, respectively; e is the electron charge constant (∼1.6 × 10^{-19} C); h is the Planck constant (∼6.62 × 10^{-34} J · s); c is the speed of light (∼3 × 10^8 m/s), and λ is the wavelength of incident light.

The effect of light irradiation at different wavelengths on the performance of the p-ZnO:Sb ⊗ n-ZnO:Ga homojunction PD

was researched. The R and D^* at −0.1 V were calculated using Eqs. (1) and (2), respectively. Figure 3(e) demonstrates that the largest R_{max} can reach 2.32 A/W at a wavelength of 360 nm; thereby, the UV/visible rejection ratio $R_{360}/R_{400} \sim 430$ was achieved, which indicates that the p-ZnO:Sb ⊗ n-ZnO:Ga homojunction PD has outstanding detection ability for UV lights, whereas the higher spectral response can be attributed to the absorption characteristics of CVD-synthesized samples. In addition, we found that the D^* reaches the maximum value of $\sim 6.5 \times 10^{13}$ Jones at 360 nm and maintains the same order of 10^{13} in a broad UV wavelength range, which is superior to most previously reported ZnO-based homojunction detectors [41]. The EQE and LDR at different wavelengths obtained from Eqs. (3) and (4) are shown in Fig. 3(f). The EQE data shows that the PD exhibits high photoelectric conversion efficiencies in the range of 300–400 nm, and the highest EQE value is achieved at the wavelength of 360 nm. The calculated LDR values are averagely evaluated to ∼60 dB at UV wavelengths of 300–400 nm, which is comparable with those of commercial photodetectors [55]. In particular, the largest LDR can raise up to 80 dB at the wavelength of 360 nm, which indicates that the fabricated detector has excellent signal-to-noise ratio.

To evaluate the photodetecting performance of the p-ZnO:Sb ⊗ n-ZnO:Ga homojunction PD under 360 nm light irradiation at −0.1 V, we performed I–V characteristics tests of the PD under different light intensities ranging from 0 to 5 mW/cm^2, as shown in Fig. 4(a). It clearly illustrates that the photocurrent exhibits an observable enhancement with increasing light intensities. The photo–dark current ratio of the PD increases from $\sim 10^3$ ($\sim$0.1 mW/cm^2) to $\sim 10^5$ at −0.1 V bias [Fig. 12(d) in Appendix F]. The robust increase of the photo–dark current ratio can be attributed to the fact that the higher intensity of the incoming lights induces more photocarriers, in turn, enhancing the photocurrent response. Figure 4(b) presents the changes of the obtained photocurrents versus the light illumination intensity of the PD at −0.1 V bias. The change can be well fitted by the power law [40]

$$I_{ph} \propto AP^{\alpha}, \tag{5}$$

where A is a constant at a specific wavelength, and α is a power-law factor. The α value is estimated to be 0.90 (ideal value is 1), suggesting that interfacial recombination loss in the homojunction could be neglected upon UV light irradiation. We also noted the linear character of the photocurrent via light illumination intensity, which is different from low-dimensional ZnO heterojunction photodiodes. Such an experimental phenomenon is mainly caused by the existence of fewer interface defects acting as the charge recombination centers in homojunction. Thus, the trapping centers are rapidly saturated upon UV light illumination, which effectively reduces recombination loss resulting from the growing concentration of photogenerated carriers in homojunction interface [39].

The illumination density-dependent photoresponse performances of the p-ZnO:Sb ⊗ n-ZnO:Ga homojunction PD were studied at the wavelength of 360 nm. Figures 4(c) and 4(d) demonstrate that the R and D^* show a decreasing trend

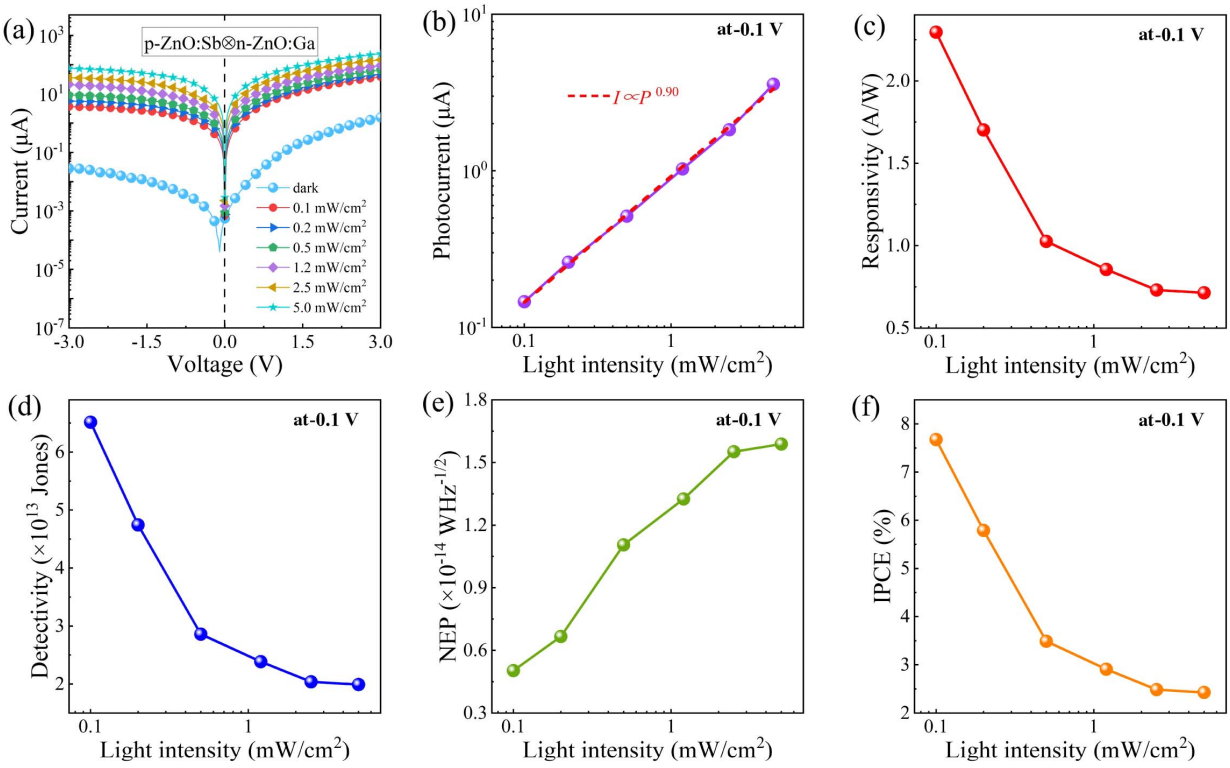

Fig. 4. Photosensitivity characterization of the p-n homojunction PD when measured under 360 nm light irradiation via different optical intensities. (a) Logarithmic I–V characteristic curves of the PD in dark and under 360 nm light source illumination with the intensities varying from 0.1 to 5.0 mW/cm^2. (b) Logarithmic plot of the photocurrent versus incident light intensity at −0.1 V bias. When evaluated at 360 nm light illumination: (c) R; (d) D^*; (e) NEP; and (f) IPCE of PD as a function of light intensity at −0.1 V bias.

when increasing the light intensity of the incident light. That is, the largest R (~2.3 A/W) and D^* (~6.5×10^{13} Jones) can be achieved under weak light density of UV irradiation, indicating the outstanding photosensitivities of the PD to weak UV light signals. The reduced visibility of the obtained photosensitive properties with increasing light intensity could be probably attributed to the surface and interfacial defects of ZnO:Sb and ZnO:Ga MWs as well as the constructed devices. In that case, a small part of the photocarriers may be recombined before being collected by electrodes, decreasing the average lifetime with the increasing carrier recombination rate [56].

The NEP and IPCE of the p-ZnO:Sb ⊗ n-ZnO:Ga homojunction PD were analyzed according to the following equations [56,57]:

$$\mathrm{NEP} = \frac{\sqrt{2eI_d}}{\mathrm{R}}, \tag{6}$$

$$\mathrm{IPCE} = \frac{1240J}{\lambda P}, \tag{7}$$

where e and I_d are the electron charge constant and dark current, respectively. J and P are the measured photocurrent density and light intensity at a fixed wavelength ($\lambda = 360$ nm). The variation of NEP as a function of different light intensities is plotted in Fig. 4(e) at −0.1 V bias. As the UV light intensity increases, the NEP increases gradually, indicating that the PD shows lower NEP (~4.8×10^{-15} W $\mathrm{Hz}^{-1/2}$) at the weak light signals. This phenomenon can be attributed to the tiny contact area between the ZnO:Sb and ZnO:Ga MWs, which effectively reduces the background noise caused by the much lower interfacial defect states. Figure 4(f) depicts the changes of IPCE versus optical densities of the incoming light, which were calculated by using Eq. (7). The observed negative relationship could be speculated to the fact that the internal gain effect of the PD diminishes with increasing UV light irradiance density [32,58]. Therefore, the PD gives a maximum IPCE of 7.8% upon the 360 nm light irradiation.

To access the stabilities of the p-ZnO:Sb ⊗ n-ZnO:Ga homojunction PD, the I–t curves of the device at different reverse voltages are displayed in Fig. 5(a). The current has a strong dependence on the reverse bias. Further, the fabricated PD shows a superior time-dependent photoresponse even at low bias along with excellent reproducibility and stability, which is considered to be a critical factor for practical application in low-power devices. The dark current and photoresponse sensitivity as a function of different reverse bias are as plotted in Fig. 5(b). The results demonstrate that the photoresponse sensitivity decreases with increasing dark currents under reverse bias condition, where the sharply increased dark current may be attributed to the avalanche multiplication of carriers in the depletion layer caused by the larger reverse bias [58]. The environmental stability of the unencapsulated p-ZnO:Sb ⊗ n-ZnO:Ga homojunction PD was tested. In the measurement, the photocurrent intensity was recorded under continuous irradiation of 360 nm light (0.1 mW/cm^2) at room temperature (25°C) and ~45% humidity. As shown in Fig. 5(c), the device has only ~10% fluctuation of photocurrent intensity after prolonged UV irradiation. Meanwhile, the inset of Fig. 5(c) shows that the environmental stability of the PD was discussed as a function of storage time (15, 30, and 60 days later). Although the photocurrent intensity fluctuated after 60 days of storage, the device also maintained over 90% of the pristine photocurrent, indicating that the device can ensure long-term stable operation even in an unencapsulated state.

The response speed of the p-ZnO:Sb ⊗ n-ZnO:Ga homojunction PD was examined by measuring its rise τ_r (10%–90%) and decay τ_d (90%–10%) upon switching the UV irradiation on and off. As shown in Fig. 12(e) in Appendix F, the τ_r and τ_d are estimated to be 0.073 and 0.392 s, respectively. The much lower response speed could result from the test limits of the semiconductor parametric analysis instrument. To actually approach the response speed, the transient photoresponse of our as-fabricated p-ZnO:Sb ⊗ n-ZnO:Ga homojunction PD was conducted under a 360 nm pulse laser illumination at −0.1 V. As shown in Fig. 12(f) in Appendix F, the captured pulse signals with steady, rapid, and repeatable photoresponse are clearly obtained. Figure 5(d) exhibits a single pulse of the time-resolved photoresponse; thereby the τ_r and τ_d can be derived to about 0.48 and 79.41 ms, respectively. The fast response speed of the PD was superior to most of previously reported ZnO-based homojunction detectors. It is mainly attributed to the cooperative effect of composite (external and built-in) electric fields at the junction interface and the formation of high-quality homojunction with fewer trap states; thus, it is conducive to the quick separation and transport of photoinduced carriers [35,59,60].

The photosensitive mechanism and photocarrier transport paths of our as-fabricated p-ZnO:Sb ⊗ n-ZnO:Ga homojunction device can be further understood by the energy band diagram, as shown in Fig. 5(e). Shown in the photograph (left), E_C, E_V, and E_F are the conduction band, valence band, and Fermi energy level of CVD-synthesized ZnO:Sb and ZnO:Ga samples, respectively. E_g and χ are their bandgap energies and electron affinity, respectively. It has been reported that the bandgap energy and electron affinity values of ZnO are 3.37 and 4.35 eV, respectively [Fig. 5(e)-I] [59]. As both MWs are in contact with each other, the difference in Fermi levels would lead to the majority carriers interdiffusion between the ZnO:Ga MW (for the electrons) and ZnO:Sb MW (for the holes). When the device is in an equilibrium state, built-in potential E_0 is established [see Fig. 5(e)-II]. The depletion layer thickness (w) created in ZnO:Sb and ZnO:Ga samples at 0 V bias can be estimated using the formula [54]

$$w = \sqrt{\frac{2\varepsilon_n\varepsilon_p\varepsilon_0 n_{\mathrm{ZnO:Sb}}E_0}{en_X(\varepsilon_n n_{\mathrm{ZnO:Ga}} + \varepsilon_p n_{\mathrm{ZnO:Sb}})}}, \tag{8}$$

where ε_p and ε_n are relative dielectric constant of ZnO:Sb and ZnO:Ga MW, respectively. n_X (X = ZnO:Sb, ZnO:Ga) is carrier densities of ZnO:Sb and ZnO:Ga MW, respectively. E_0 is the built-in field intensity of the PD, e is the elementary charge, and ε_0 is vacuum dielectric constant. The w of ZnO:Sb and ZnO:Ga MW are estimated to be ~8.16 and ~2.63 nm, respectively. The depletion layer thickness of the p-ZnO:Sb ⊗ n-ZnO:Ga homojunction PD is about 10.79 nm at 0 V bias. However, once the PD is operated upon UV light illumination at −0.1 V bias, photoinduced generation of electron-hole pairs

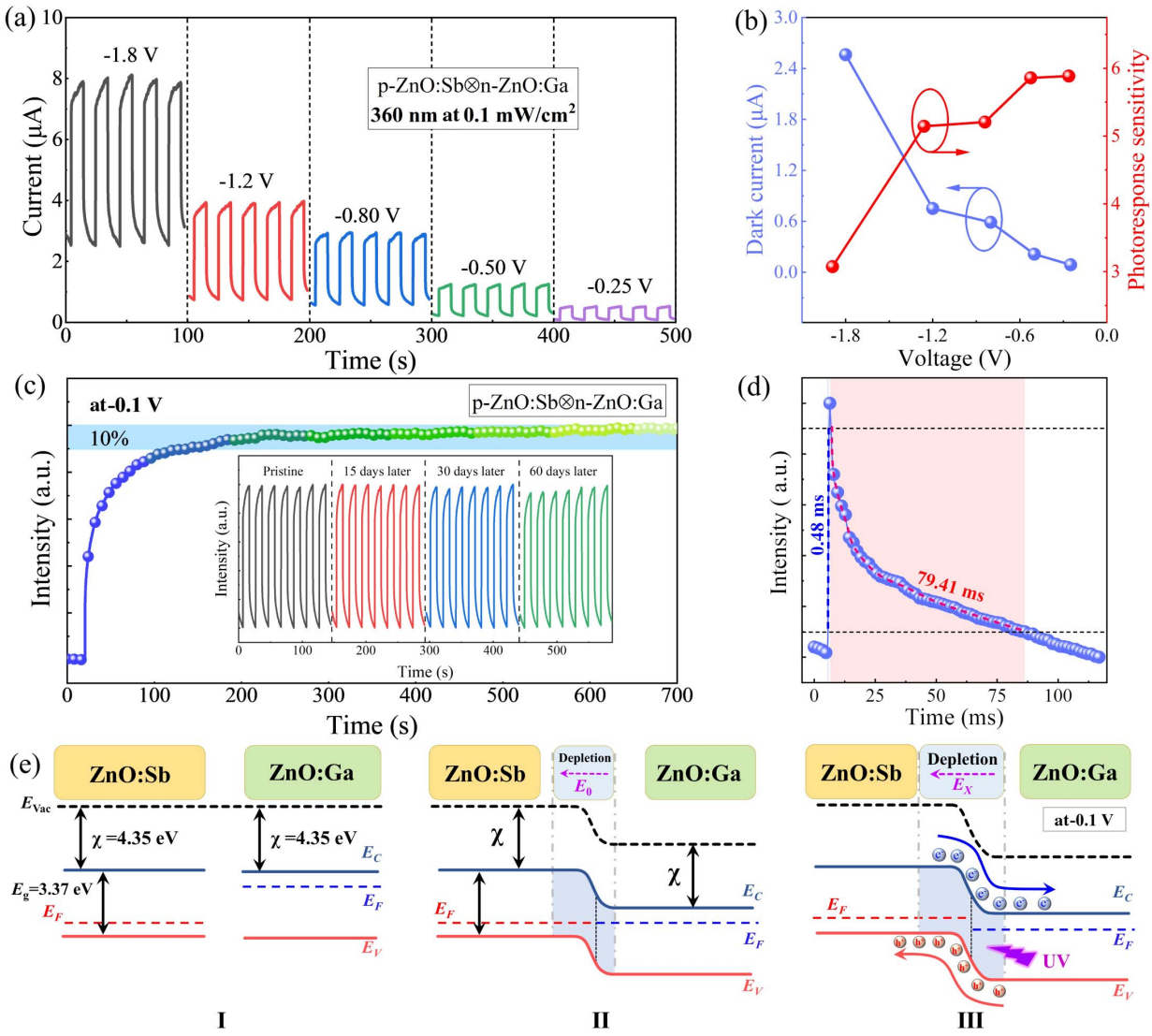

Fig. 5. Device stability and photosensitive mechanism of our constructed p-ZnO:Sb⊗n-ZnO:Ga MWs homojunction PD. (a) Bias-dependent *I*–*t* characteristic curves of the PD device under 360 nm light irradiation via 0.1 mW/cm^2. (b) Changes of dark currents and photoresponse sensitivity versus the applied bias voltages when operated under 360 nm light illumination via 0.1 mW/cm^2. (c) Normalized photocurrent intensity of the UV PD under irradiation of 360 nm light at −0.1 V bias. The inset is the stability of UV PD as a function of storage time. (d) Photoresponse speed to 360 nm pulse laser with a modulation frequency of 10 Hz at −0.1 V bias. (e) Energy band diagram of the p-n homojunction PD.

will be formed in the depletion layer and then could be separated by combining the external electric field and the built-in electric field [Fig. 5(e)-III]. In this case, the external electric-field associated with the preformed built-in potential is more favorable for photocarriers transport. As summarized in Table 2, the p-ZnO:Sb ⊗ n-ZnO:Ga homojunction PD in this research exhibits much better photosensitive performance than other previously reported ZnO-based UV PDs.

The potential application of the p-ZnO:Sb ⊗ n-ZnO:Ga homojunction PD in flexible integrated optoelectronic devices was further researched. The schematic architecture of the flexible integrated homojunction array based on a single unit of our preprepared p-ZnO:Sb ⊗ n-ZnO:Ga homojunction device is illustrated in Fig. 6(a). We fabricated an array unit of the PD in a 500 μm × 700 μm area. First, Au electrodes were deposited on the flexible PET substrate, then ZnO:Sb MW and ZnO:Ga MW were welded on the Au electrodes by indium, and finally the device was simply covered with polymethyl methacrylate (PMMA). Figure 6(b) represents the optical photograph of a flexible integrated PD array unit on PET substrate; the corresponding microscopic photograph is shown in Fig. 6(c). The microscopic photograph of the device shows that all the ZnO:Ga MWs form good contacts with ZnO:Sb MWs. Meanwhile, to study the stability of the PD array unit under harsh conditions, the photocurrents of the device were measured after it was subjected to various bending angles and bending cycles, as shown in Figs. 13(a)–13(e) in Appendix G. It demonstrates that the photocurrent of the fabricated PD array unit remained fairly stable up to 30° bending angles and 50 bending cycles, keeping more than 80% of its initial

Table 2. Comparison of Detection Performance Parameters of the ZnO-Based UV PDs

Photodetectors	Wavelength, Power	Bias (V)	τ_r/τ_d	R (A/W)	D^* (Jones)	Refs.
Au-ZnO-Au	365 nm, 250 mW/cm^2	1	3.3 s/20 s	0.01	5×10^{10}	[33]
ZnO (2D)/GaN (1D)	352 nm, 20 mW/cm^2	1	—	0.34	9.76×10^{9}	[34]
ZnO:Sb/ZnO nanowire	365 nm, 0.3 mW/cm^2	0	30 ms/30 ms	—	—	[35]
ZnO QD/ZnO film	350 nm, 1.72 mW/cm^2	10	1.56 s/1.82 s	1.63	11.4×10^{11}	[41]
ZnO:Sb MW/ZnO MW	386 nm, —	−5	—	0.2	—	[43]
ZnO:Ag nanowire	350 nm, 15–20 mW/cm^2	0	1.09 s/5 s	—	—	[61]
ZnO nanofibers	360 nm, 2.5 mW/cm^2	0	3.90 s/4.71 s	0.001	—	[62]
Carbon-ZnO film-carbon	365 nm, 0.1 mW/cm^2	1	62.6 s/30.1 s	—	—	[63]
ZnO:Sb/ZnO nanorod	365 nm, 60 mW/cm^2	−3	15.2 s/20.3 s	—	—	[64]
Au-ZnO nanofiber-Au	350 nm, 0.753 mW/cm^2	5	19.5 s/45.2 s	—	—	[65]
ZnO/NiO nanofiber	350 nm, 0.753 mW/cm^2	0	7.5 s/4.8 s	4×10^{-4}	—	[65]
p-ZnO:Sb⊗n-ZnO:Ga	360 nm, 0.1 mW/cm^2	−0.1	0.48 ms/79.41 ms	2.3	6.5×10^{13}	This work

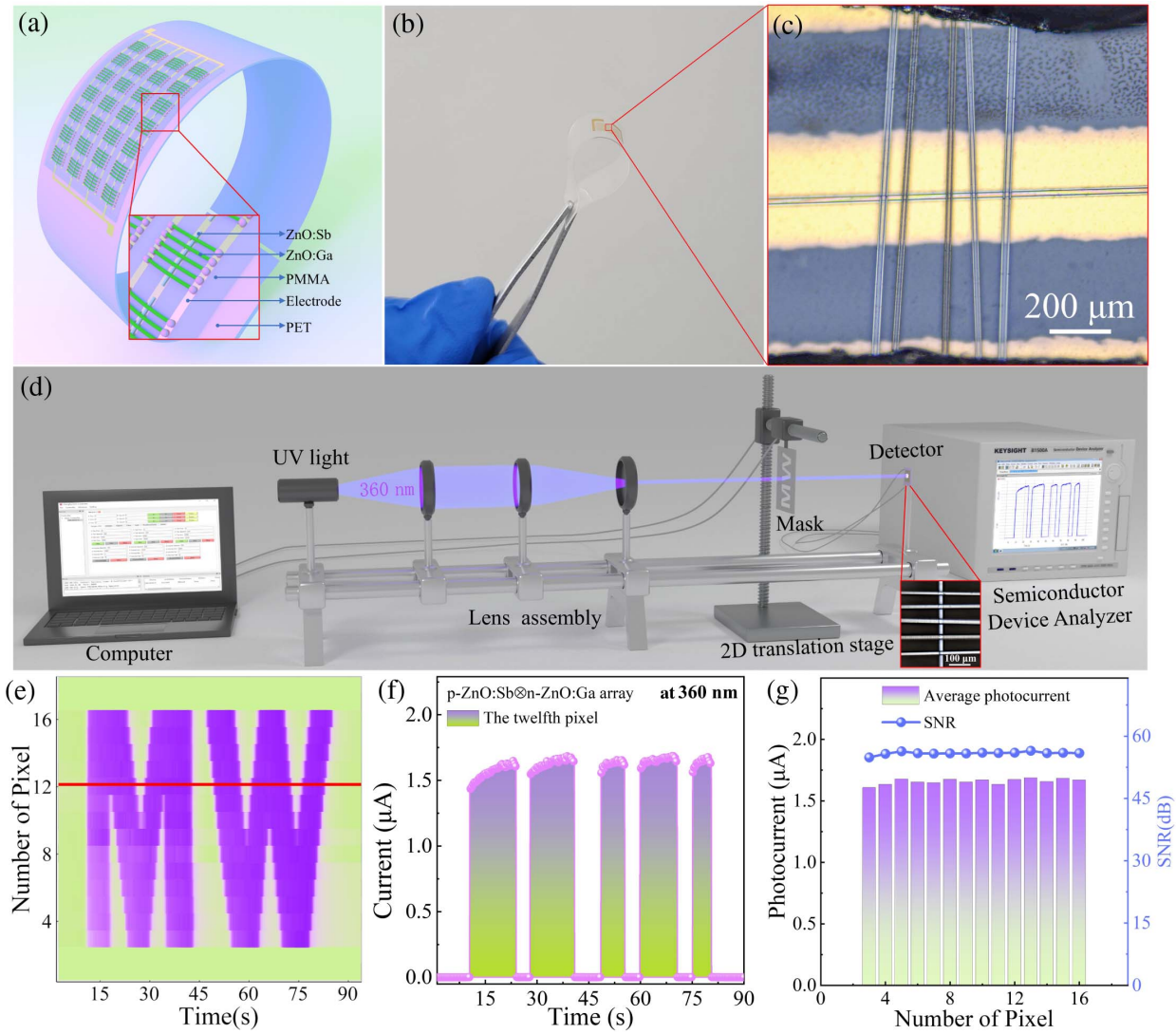

Fig. 6. Photoimaging application of our fabricated p-ZnO:Sb⊗n-ZnO:Ga an MWs homojunction UV PD. (a) Schematic design of the flexible integrated p-n homojunction array UV PD. (b) Optical photograph of a flexible MW homojunction array on PET substrate. (c) Microscopic image of a flexible MWs homojunction array. Scale bar: 200 μm. (d) Schematic diagram of the photoimaging measurement system. Inset in bottom right corner shows microscopic image of p-n homojunction array. Scale bar: 100 μm. (e) Imaging results of the optical patterns "MW" under 360 nm light source illumination. (f) Current waveform of the twelfth pixel acquired by the array unit. (g) Average photocurrents and signal-to-noise ratio under UV light illumination for the array unit.

photocurrent value even after 90° bending angles and 400 bending cycles. This reveals the potential of the PD array unit for versatile applications in flexible and integrated optoelectronic devices.

Finally, the proposed p-ZnO:Sb ⊗ n-ZnO:Ga homojunction PD has great potential for single pixel photoimaging, which is important functional components for information communication, image sensors, and flexible optoelectronic devices. However, high-performance flexible p-n homojunction PD with high resolution and stable photoresponse still need to be developed. Figure 6(d) shows the schematic diagram of the MW imaging measurement platform, which consists of the PD array unit, light source, lens assembly, 2D translation stage, and so on. Figure 6(e) shows an efficiently detected image of the "MW" letters collected by the array unit under 360 nm light source illumination at 0.1 mW/cm^2. Obviously, the device exhibits high contrast and resolution with sharp edges. As shown in Fig. 6(f), the current waveform of the twelfth pixel [position of the red line in Fig. 6(e)] is acquired by the array unit, which suggests that the device has the ability to track rapidly varied light signals. The average photocurrent and SNR of the device were obtained under different scanned pixels, as demonstrated in Fig. 6(g). The imaging results clearly indicate the excellent imaging capability and superior signal current uniformity of the device as a single sensing pixel. It is notable that the SNR of the array unit is all more than 50 dB, and the high SNR values reveal the outstanding low-light detection capability of the device, suggesting that the homojunction array unit can efficiently convert UV light into photocurrents. Therefore, the p-ZnO:Sb ⊗ n-ZnO:Ga homojunction PD as a UV signal receiving terminal can provide new ideas for the design and fabrication of miniaturized, low-power, and high-performance flexible integrated UV imaging sensor devices.

4. CONCLUSIONS

In summary, we have successfully constructed a high-performance flexible UV PD based on a p-ZnO:Sb ⊗ n-ZnO:Ga MWs homojunction. The device can work at a relatively low operation voltage, suggesting its low-power consumption detection. The PD exhibits an impressive overall photosensitive property, including a largest responsivity of 2.3 A/W, a large specific detectivity of 6.5×10^{13} Jones, a superior NEP of 4.8×10^{-15} W $Hz^{-1/2}$, an excellent IPCE of 7.8%, and fast response speed (0.48 ms/79.41 ms) under 360 nm light illumination at −0.1 V. These comparable figure-of-merit parameters show that the homojunction device demonstrates its remarkable potential for UV imaging, optical communication, and biological detection. As a unit of p-ZnO:Sb ⊗ n-ZnO:Ga MWs homojunction was integrated into a flexible array, the device exhibits less than 20% degradation in photodetection performance after 90° angles and 400 times bending-releasing test, indicating its good mechanical flexibility and stability. Moreover, the fabricated PD array unit was also integrated into a string array pixel, giving rise to high-resolution imaging capabilities. Given their UV photodetection properties, excellent mechanical flexibility and stability, and photosensitive imaging, we believe that the as-constructed p-ZnO:Sb ⊗ n-ZnO:Ga MWs homojunction PD will boost the progress toward next-generation wearable technologies and integrated UV imaging sensor.

APPENDIX A: SCHEMATIC VIEW OF FIELD-EFFECT TRANSISTORS

Figure 7 shows the schematic diagram of the FET device structure, including a single microwire, source and drain electrodes, and the global back gate electrode.

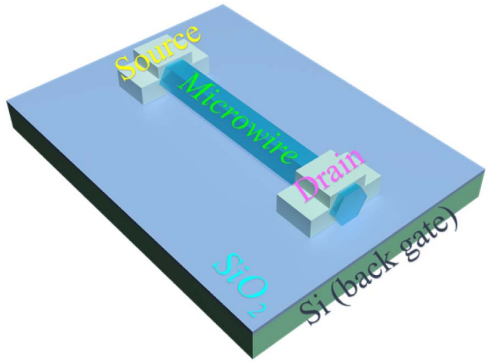

Fig. 7. Schematic illustration of the single MW-based FET.

APPENDIX B: CONSTRUCTION PROCESS OF DEVICE

Figure 8 presents the detail information on the process of photodetection device fabrication.

APPENDIX C: PHOTOGRAPH OF CVD-PREPARED MWs

Figure 9 illustrates optical photographs of CVD-prepared ZnO:Ga and ZnO:Sb MWs, the enlarged wire samples, and a microscope photograph of a single MW bent through 180°.

APPENDIX D: ELECTRICAL CHARACTERISTICS OF DEVICE AND MWs

Figure 10 demonstrates the rectification characteristics of the constructed homojunction device, the microscopic photograph of the corresponding device, and the *I-V* characteristic curves of the ZnO:Sb and ZnO:Ga MWs, respectively.

APPENDIX E: THERMAL IMAGE AND DARK CURRENT OF DEVICE

Figure 11 displays the thermal images of the constructed homojunction devices at different conduction temperatures (from 260 to 330 K), and the dark current versus voltage plots of the devices.

APPENDIX F: ABSORPTION OF MWs AND PERFORMANCE OF DEVICE

Figure 12 exhibits the absorption versus wavelength (λ) for ZnO:Ga and ZnO:Sb MW samples, the light-to-dark current

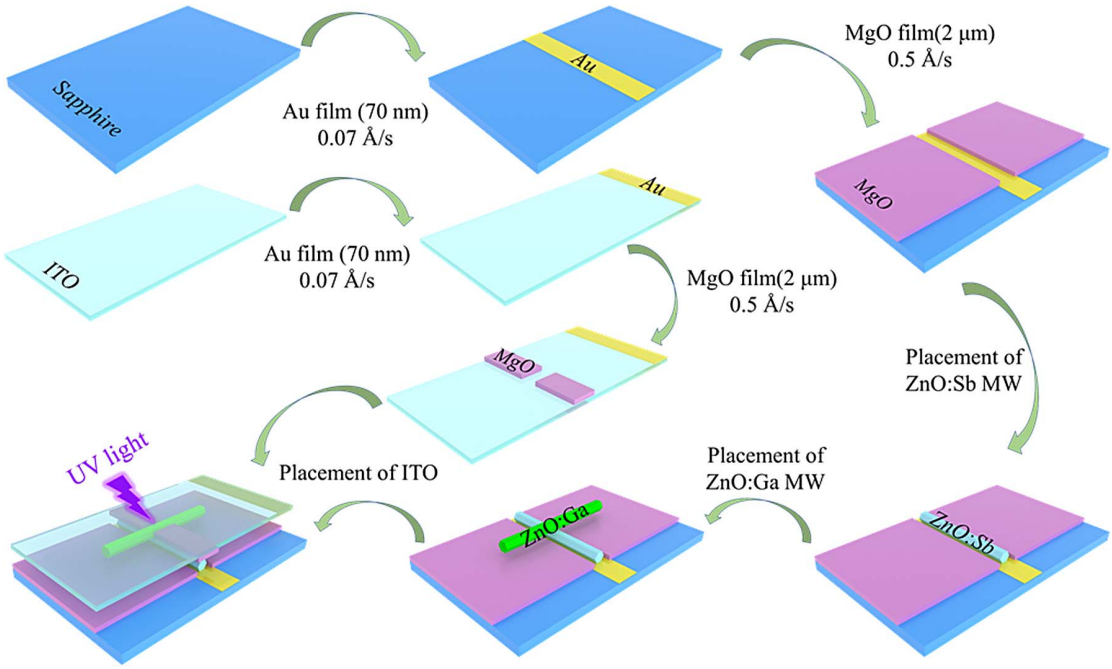

Fig. 8. Schematic illustration of the fabrication process for the p-ZnO:Sb ⊗ n-ZnO:Ga homojunction detectors.

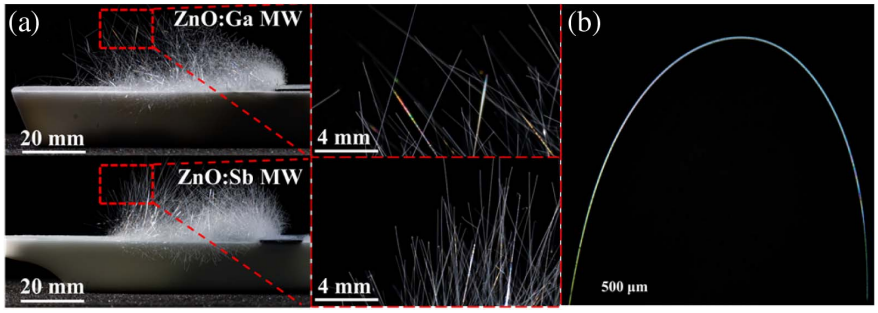

Fig. 9. (a) Optical photograph of CVD-synthesized ZnO:Ga and ZnO:Sb MWs. (b) Microscopic image of MW under 180° bending angles.

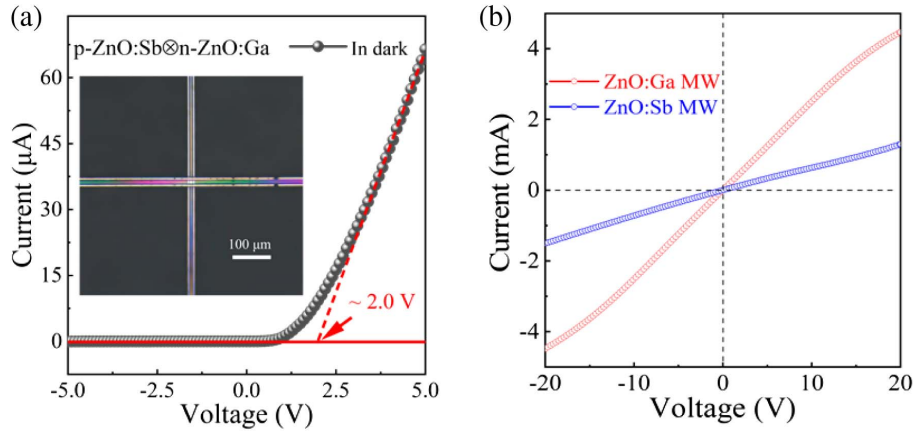

Fig. 10. (a) Typical *I-V* characteristic curve of the device. Inset shows the microscopic image of the crossed MWs device. Scale bar: 100 μm. (b) Typical *I-V* characteristic curves of ZnO:Sb MW and ZnO:Ga MW.

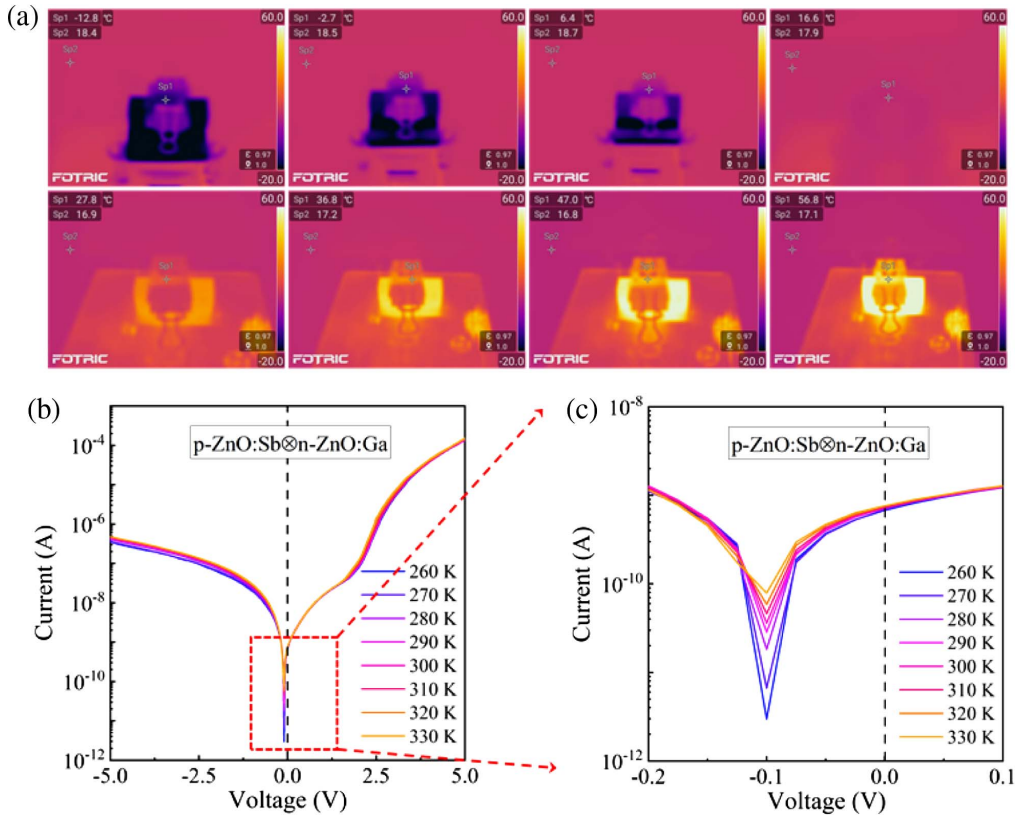

Fig. 11. (a) Thermal imaging plot. (b) Dark current curves. (c) Dark current localized magnification curves of the device at different temperature conditions.

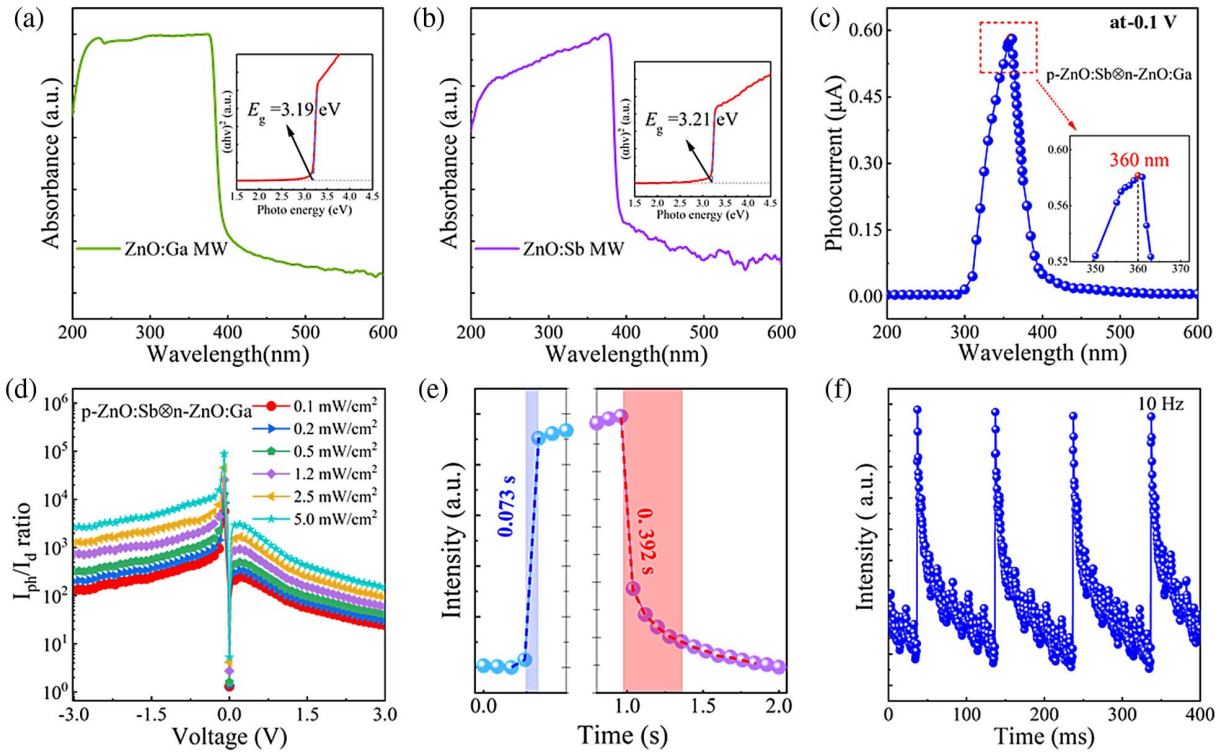

Fig. 12. Absorption versus wavelength (λ) plots of (a) ZnO:Ga MW and (b) ZnO:Sb MW. Inset is the Tauc curve from the corresponding absorption versus wavelength plots of ZnO:Ga MW and ZnO:Sb MW. (c) Photocurrent versus wavelength (λ) plots of the device at −0.1 V bias voltage. (d) Variation of photo-to-dark-current ratio I_{ph}/I_d of ZnO homojunction device at different UV light intensities. (e) Typical photoresponse of the device to 360 nm light source. (f) Typical pulse response of the device to 360 nm pulse laser.

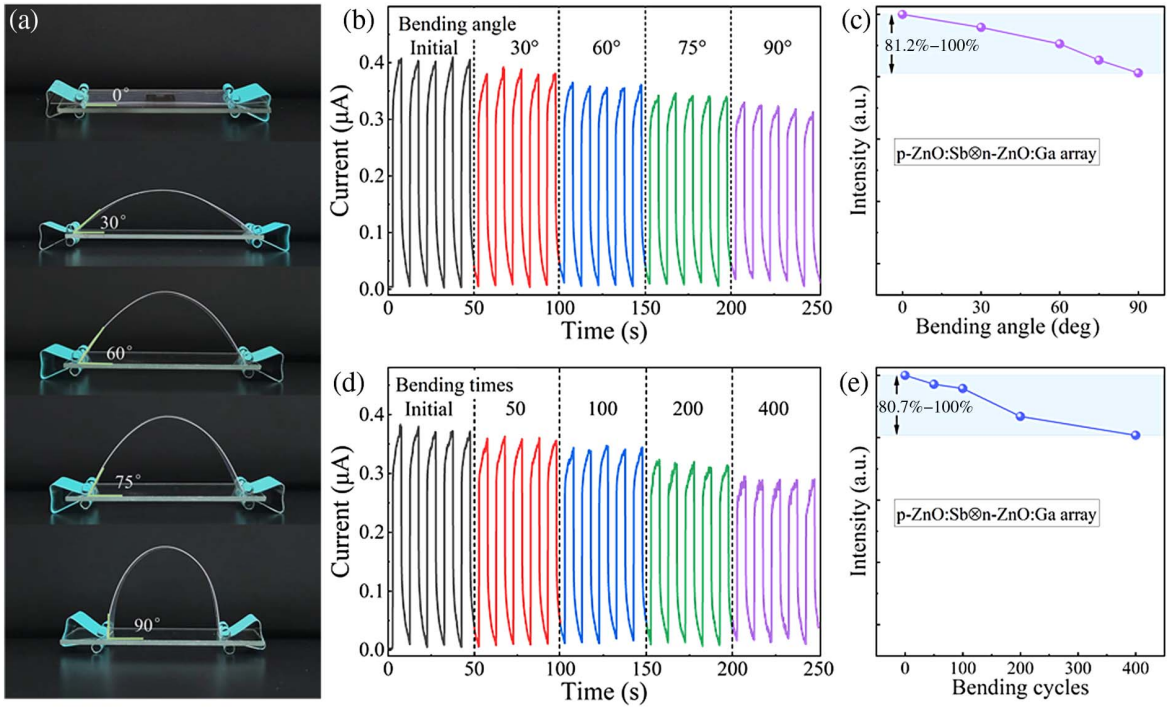

Fig. 13. (a) Optical images of the ZnO homojunction array unit with various bending angles ranging from 0° to 90°. (b) I–t curves of the ZnO homojunction array unit under varied bending angles (the light illumination wavelength is 360 nm), and the corresponding light intensity is fixed at 0.2 mW/cm^2. (c) Bending angle-dependent photocurrents. (d) I–t curves of the ZnO homojunction array unit with an increase of the bending cycles. (e) Variation of photocurrent with the increasing bending cycles.

ratio, and the response speed of the p-ZnO:Sb⊗n-ZnO:Ga MW homojunction device.

APPENDIX G: FLEXIBILITY OF DEVICE

Figure 13 shows the optical images of the constructed homojunction array unit at different bending angles (0° to 90°), the I–t curves for different bending angles and bending times.

Funding. Postgraduate Research & Practice Innovation Program of Jiangsu Province (KYCX23_0348); Funding for Outstanding Doctoral Dissertation in Nanjing University of Aeronautics and Astronautics (BCXJ22-14); Fundamental Research Funds for the Central Universities (NC2022008); National Natural Science Foundation of China (11974182, 12374257).

Disclosures. The authors declare no conflicts of interest.

Data Availability. The data that support the findings of this study are available from the corresponding author upon reasonable request.

REFERENCES

1. T. Xu, M. M. Jiang, P. Wan, *et al.*, "Bifunctional ultraviolet light-emitting/detecting device based on a SnO_2 microwire/p-GaN heterojunction," Photon. Res. **9**, 2475–2485 (2021).
2. C. H. Gong, J. W. Chu, S. F. Qian, *et al.*, "Large-scale ultrathin 2D wide-bandgap BiOBr nanoflakes for gate-controlled deep-ultraviolet phototransistors," Adv. Mater. **32**, 1908242 (2020).
3. Z. S. Xu, X. Han, W. Q. Wu, *et al.*, "Controlled on-chip fabrication of large-scale perovskite single crystal arrays for high-performance laser and photodetector integration," Light Sci. Appl. **12**, 67 (2023).
4. Z. Zheng, L. Gan, J. B. Zhang, *et al.*, "An enhanced UV-Vis-NIR and flexible photodetector based on electrospun ZnO nanowire array/PbS quantum dots film heterostructure," Adv. Sci. **4**, 1600316 (2017).
5. H. J. He, L. Jiang, Y. Pan, *et al.*, "Integrated sensing and communication in an optical fibre," Light Sci. Appl. **12**, 25 (2023).
6. Y. Zhang, F. Cao, S. Y. Li, *et al.*, "Integration of filter membrane and $Ca_2Nb_3O_{10}$ nanosheets for high performance flexible UV photodetectors," J. Mater. Sci. Technol. **129**, 108–114 (2022).
7. R. J. Tian, X. T. Gan, C. Q. Li, *et al.*, "Chip-integrated van der Waals PN heterojunction photodetector with low dark current and high responsivity," Light Sci. Appl. **11**, 101 (2022).
8. D. Wang, P. Shi, R. F. Xing, *et al.*, "Self-powered ZnO/SrCoOx flexible ultraviolet detectors processed at room temperature," Mater. Des. **203**, 109616 (2021).
9. W. H. Ding and X. Q. Meng, "High performance solar-blind UV detector based on β-Ga_2O_3/GaN nanowires heterojunction," J. Alloys Compd. **866**, 157564 (2021).
10. M. Tan, M. Li, W. Pan, *et al.*, "Carbonized polymer dots enhanced stability and flexibility of quasi-2D perovskite photodetector," Light Sci. Appl. **11**, 304 (2022).
11. D. S. Schneider, A. Bablich, and M. C. Lemme, "Flexible hybrid graphene/a-Si:H multispectral photodetectors," Nanoscale **9**, 8573–8579 (2017).
12. R. S. Veerla, P. Sahatiya, and S. Badhulika, "Fabrication of a flexible UV photodetector and disposable photoresponsive uric acid sensor by direct writing of ZnO pencil on paper," J. Mater. Chem. C **5**, 10231–10240 (2017).
13. J. Hu, S. Yang, Z. Zhang, *et al.*, "Solution-processed, flexible and broadband photodetector based on $CsPbBr_3$/PbSe quantum dot heterostructures," J. Mater. Sci. Technol. **68**, 216–226 (2021).
14. L. Chen, C. T. Yang, and C. Y. Yan, "High-performance UV detectors based on 2D CVD bismuth oxybromide single-crystal nanosheets," J. Mater. Sci. Technol. **48**, 100–104 (2020).

15. M. Tan, C. Hu, Y. Lan, *et al.*, "2D lead dihalides for high-performance ultraviolet photodetectors and their detection mechanism investigation," Small **13**, 1702024 (2017).
16. L. Peng, L. Hu, and X. Fang, "Low-dimensional nanostructure ultraviolet photodetectors," Adv. Mater. **25**, 5321–5328 (2013).
17. M. Shahid, J. Cheng, T. Li, *et al.*, "High photodetectivity of low-voltage flexible photodetectors assembled with hybrid aligned nanowire arrays," J. Mater. Chem. C **6**, 6510–6519 (2018).
18. Y. F. Li, J. Feng, and H. B. Sun, "Perovskite quantum dots for light-emitting devices," Nanoscale **11**, 19119–19139 (2019).
19. J. D. Lin, Y. X. Lu, X. Li, *et al.*, "Perovskite quantum dots glasses based backlit displays," ACS Energy Lett. **6**, 519–528 (2021).
20. T. Hacıefendioğlu, T. K. Solmaz, M. Erkan, *et al.*, "A comprehensive approach for the instability of PbTe quantum dots and design of a combinatorial passivation strategy," Sol. Energy Mater. Sol. Cells **207**, 110362 (2020).
21. M. S. de la Fuente, S. Kaur, Q. Hu, *et al.*, "Enhanced charge carrier transport in 2D perovskites by incorporating single-walled carbon nanotubes or graphene," ACS Energy Lett. **5**, 109–116 (2019).
22. V. Q. Dang, T. Q. Trung, D. I. Kim, *et al.*, "Ultrahigh responsivity in graphene-ZnO nanorod hybrid UV photodetector," Small **11**, 3054–3065 (2015).
23. Q. Cai, H. You, H. Guo, *et al.*, "Progress on AlGaN-based solar-blind ultraviolet photodetectors and focal plane arrays," Light Sci. Appl. **10**, 94 (2021).
24. A. K. Ranade, R. D. Mahyavanshi, P. Desai, *et al.*, "Ultraviolet light induced electrical hysteresis effect in graphene-GaN heterojunction," Appl. Phys. Lett. **114**, 151102 (2019).
25. C. L. Hsu, H. H. Li, and T. J. Hsueh, "Water- and humidity-enhanced UV detector by using p-type La-doped ZnO nanowires on flexible polyimide substrate," ACS Appl. Mater. Interfaces **5**, 11142–11151 (2013).
26. A. Gundimeda, S. Krishna, N. Aggarwal, *et al.*, "Fabrication of non-polar GaN based highly responsive and fast UV photodetector," Appl. Phys. Lett. **110**, 103507 (2017).
27. B. Uppalapati, D. Gajula, F. Bayram, *et al.*, "An AlGaN/GaN dual channel triangular microcantilever based UV detector," ACS Photon. **9**, 1908–1918 (2022).
28. S. Veeralingam, L. Durai, P. Yadav, *et al.*, "Record-high responsivity and detectivity of a flexible deep-ultraviolet photodetector based on solid state-assisted synthesized hBN nanosheets," ACS Appl. Electron. Mater. **3**, 1162–1169 (2021).
29. Q. H. Li, Y. Liu, X. M. Guan, *et al.*, "High-performance ultraviolet photodetector based on p-PEDOT:PSS film/p-ZnO:Sb microwire/n-Si double heterojunction," Ceram. Int. **49**, 8302–8312 (2023).
30. G. D. Yuan, W. J. Zhang, J. S. Jie, *et al.*, "Tunable n-type conductivity and transport properties of Ga-doped ZnO nanowire arrays," Adv. Mater. **20**, 168–173 (2008).
31. G. Jang, S. J. Lee, D. Lee, *et al.*, "Flexible UV detector based on carbon fibers, ZnO nanorods, and Ag nanowires," J. Mater. Chem. C **5**, 4537–4542 (2017).
32. C. Soci, A. Zhang, B. Xiang, *et al.*, "ZnO nanowire UV photodetectors with high internal gain," Nano Lett. **7**, 1003–1009 (2007).
33. S. Kiruthika, S. Singh, and G. U. Kulkarni, "Large area transparent ZnO photodetectors with Au wire network electrodes," RSC Adv. **6**, 44668–44672 (2016).
34. D. J. Lee, S. R. Ryu, G. M. Kumar, *et al.*, "Piezo-phototronic effect triggered flexible UV photodetectors based on ZnO nanosheets/GaN nanorods arrays," Appl. Surf. Sci. **558**, 149896 (2021).
35. Y. Wang, Y. Chen, W. Zhao, *et al.*, "A self-powered fast-response ultraviolet detector of p-n homojunction assembled from two ZnO-based nanowires," Nano-micro Lett. **9**, 11 (2017).
36. Y. Huang, X. F. Duan, Y. Cui, *et al.*, "Gallium nitride nanowire nanodevices," Nano Lett. **2**, 101–104 (2002).
37. Q. Cui, Y. Hu, C. Zhou, *et al.*, "Single crystal microwires of p-DTS $(FBTTh_2)_2$ and their use in the fabrication of field-effect transistors and photodetectors," Adv. Funct. Mater. **28**, 1702073 (2017).
38. L. Luo, Y. Huang, K. Cheng, *et al.*, "MXene-GaN van der Waals metal-semiconductor junctions for high performance multiple quantum well photodetectors," Light Sci. Appl. **10**, 177 (2021).
39. C. Thota, G. Murali, R. Dhanalakshmi, *et al.*, "2D MXene/1D GaN van der Waals heterojunction for self-powered UV photodetector," Appl. Phys. Lett. **122**, 031102 (2023).
40. W. Song, J. Chen, Z. Li, *et al.*, "Self-powered MXene/GaN van der Waals heterojunction ultraviolet photodiodes with superhigh efficiency and stable current outputs," Adv. Mater. **33**, 2101059 (2021).
41. Z. Li, X. Yu, Y. Zhu, *et al.*, "High performance ZnO quantum dot (QD)/magnetron sputtered ZnO homojunction ultraviolet photodetectors," Appl. Surf. Sci. **582**, 152352 (2022).
42. S. Bai, W. Wu, Y. Qin, *et al.*, "High-performance integrated ZnO nanowire UV sensors on rigid and flexible substrates," Adv. Funct. Mater. **21**, 4464–4469 (2011).
43. L. Shi, F. Wang, B. Li, *et al.*, "A highly efficient UV photodetector based on a ZnO microwire p–n homojunction," J. Mater. Chem. C **2**, 5005–5010 (2014).
44. Y. C. Lu, Z. F. Zhang, X. Yang, *et al.*, "High-performance solar-blind photodetector arrays constructed from Sn-doped Ga_2O_3 microwires via patterned electrodes," Nano Res. **15**, 7631–7638 (2022).
45. C. M. Yang, M. H. Hon, and I. C. Leu, "Patterned Zn-seeds and selective growth of ZnO nanowire arrays on transparent conductive substrate and their field emission characteristics," Ceram. Int. **38**, 4277–4283 (2012).
46. C. L. Hsu, Y. H. Lin, L. K. Wang, *et al.*, "Tunable UV- and visible-light photoresponse based on p-ZnO nanostructures/n-ZnO/glass peppered with Au nanoparticles," ACS Appl. Mater. Interfaces **9**, 14935–14944 (2017).
47. M. Liu, M. Jiang, Q. Zhao, *et al.*, "Ultraviolet exciton-polariton light-emitting diode in a ZnO microwire homojunction," ACS Appl. Mater. Interfaces **15**, 13258–13269 (2023).
48. Y. Liu, M. Jiang, P. Wan, *et al.*, "Enhanced performance of ZnO microwire/PEDOT:PSS heterojunction ultraviolet photodetectors via carbon nanohorns and DMSO treatment," J. Mater. Chem. C. **10**, 12809–12820 (2022).
49. K. Tang, M. Jiang, B. Yang, *et al.*, "Enhancing UV photodetection performance of an individual ZnO microwire p-n homojunction via interfacial engineering," Nanoscale. **15**, 2292–2304 (2023).
50. X. F. Duan, Y. Huang, Y. Cui, *et al.*, "Indium phosphide nanowires as building blocks for nanoscale electronic and optoelectronic devices," Nature **409**, 66–69 (2001).
51. Z. He, J. Jie, W. Zhang, *et al.*, "Tuning electrical and photoelectrical properties of CdSe nanowires via indium doping," Small **5**, 345–350 (2009).
52. J. Huang, C. Zhao, B. Nie, *et al.*, "High-performance mid-wavelength InAs avalanche photodiode using $AlAs_{0.13}Sb_{0.87}$ as the multiplication layer," Photon. Res. **8**, 755–759 (2020).
53. F. Cao, L. Su, T. Yan, *et al.*, "Pine-branch-like SnO_2/ZnO heterostructure with suppressed dark current and enhanced on/off ratio for visible-blind UV imaging," Adv. Electron. Mater. **8**, 2101373 (2022).
54. X. Wan, Y. Xu, H. Guo, *et al.*, "A self-powered high-performance graphene/silicon ultraviolet photodetector with ultra-shallow junction: breaking the limit of silicon?" npj 2D Mater. Appl. **1**, 4 (2017).
55. L. Su, Y. Zuo, and J. Xie, "Scalable manufacture of vertical p-GaN/n-SnO_2 heterostructure for self-powered ultraviolet photodetector, solar cell and dual-color light emitting diode," InfoMat. **3**, 598–610 (2020).
56. C. Wei, J. Xu, S. Shi, *et al.*, "Self-powered visible-blind UV photodetectors based on p-NiO nanoflakes/n-ZnO nanorod arrays with an MgO interfacial layer," J. Mater. Chem. C **7**, 9369–9379 (2019).
57. C. Xie, Y. Wang, S. Wang, *et al.*, "$Ti_3C_2T_x$ MXene/Ge 2D/3D van der Waals heterostructures as highly efficient and fast response near-infrared photodetectors," Appl. Phys. Lett. **120**, 141103 (2022).
58. C. Xie and F. Yan, "Flexible photodetectors based on novel functional materials," Small **13**, 1701822 (2017).
59. D. Kuang, A. H. Kitai, and Z. Yu, "ZnO nanowire network/4H-SiC heterojunction for improved performance ultraviolet photodetector: the effect of different SiC doping concentrations on photoresponse properties," Mater. Today Commun. **35**, 105712 (2023).

60. H. Wang, J. Ma, L. Cong, *et al.*, "Piezoelectric effect enhanced flexible UV photodetector based on Ga_2O_3/ZnO heterojunction," Mater. Today Phys. **20**, 100464 (2021).
61. O. Lupan, V. Cretu, V. Postica, *et al.*, "Silver-doped zinc oxide single nanowire multifunctional nanosensor with a significant enhancement in response," Sens. Actuators B **223**, 893–903 (2016).
62. Y. Ning, Z. Zhang, F. Teng, *et al.*, "Novel transparent and self-powered UV photodetector based on crossed ZnO nanofiber array homojunction," Small **14**, e1703754 (2018).
63. Q. Xu, L. Cheng, L. Meng, *et al.*, "Flexible self-powered ZnO film UV sensor with a high response," ACS Appl. Mater. Interfaces **11**, 26127–26133 (2019).
64. W. Dai, X. Pan, S. Chen, *et al.*, "ZnO homojunction UV photodetector based on solution-grown Sb-doped p-type ZnO nanorods and pure n-type ZnO nanorods," RSC Adv. **5**, 6311–6314 (2015).
65. Z. Zhang, Y. Ning, and X. Fang, "From nanofibers to ordered ZnO/NiO heterojunction arrays for self-powered and transparent UV photodetectors," J. Mater. Chem. C **7**, 223–229 (2019).